UMERC+OREC
2025 Conference

12-14 August | Corvallis, OR USA

Development and Validation of an Inverted Pendulum Wave Energy Converter Model

Elaine Liu[1 a], Jantzen Lee[b], Ryan G. Coe[b]

[a]*Stanford University, Stanford, CA 94305, US*
[b]*Sandia National Laboratories, Albuquerque, NM 87123, US*

Abstract

This paper describes the theory and validation of a numerical model for an inverted pendulum based wave energy converter to power oceanographic buoys. Governing equations of motion are derived to obtain linear and nonlinear models of this configuration. The parameters of the numerical models are fine tuned through system identification using experimental data from a bench test. To compare the linear and nonlinear model, varying frequencies and amplitudes were input in the two models to evaluate root mean square error differences. Additional metrics, such as total harmonic distortion, were used to quantify the nonlinearities captured in the nonlinear model. Results showed significant nonlinearities at near-zero frequency and amplitude excitations, suggesting that static and Coulomb friction play a pronounced role for these inputs. The linear model generally approximated the nonlinear model well, but exhibited a lower degree of accuracy at high amplitudes and frequencies near resonance (i.e., when response amplitudes were largest). This work provides valuable insight into modeling the dynamics of wave energy converters to allow for rapid design optimization. In quantifying conditions where the linear model sufficiently approximates the nonlinear model, future design iterations can apply the linear model to reduce computation complexity in assessing device behavior. Future work will involve improving the inverted pendulum model and investigating additional nonlinearities that may arise in a full-scale model.

Keywords: wave energy converters; inverted pendulum; nonlinear dynamics modeling; system identification

[1]∗ Corresponding author..
E-mail address: ejl2401@stanford.edu

1 Introduction

The Coastal Pioneer Array is a coastal observatory deployed as part of the Ocean Observation Initiative (OOI) supported by National Science Foundation (NSF) funding [1]. This observatory studies shelf break exchange processes and the warming of the continental shelf through a suite of oceanographic observation tools, such as buoys, gliders, and autonomous underwater vehicles that provide continuous, high resolution time-series monitoring. The Coastal Surface Moorings (CSMs) are instrumented buoy systems that form a subset of the array. These systems obtain near-surface and near-bottom measurements of the deployment site. Each CSM consists of instrumented anchor frames Multi-Functional Nodes (MFNs) on the sea floor, Near Surface Instrument Frames (NSIFs) positioned about seven meters below the water surface, and surface buoys [2, 3]. The CSMs are designed to provide power from the surface to the seafloor instrumentation through electro-mechanical (EM) cables and specially designed junctions for power and data transmission. A compliant stretch-hose connects the MFNs and NSIFs, while a fixed-length wiring chain connects the NSIFs to the surface buoy (Figure 1).

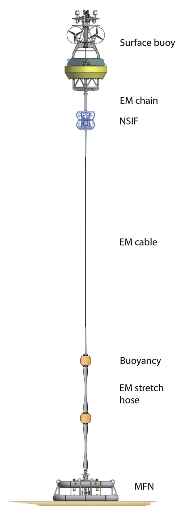

Figure 1: Schematic diagram of the Coastal Surface Moorings (CSMs) used in the Pioneer Array. CSMs include power generation on the surface buoy, a Near Surface Instrument Frame (NSIF) at 7 m depth, an electro-mechanical (EM) cable and stretch hoses extending to a Multi-Function Node (MFN) [1].

To power the array of sensors in the CSMs, the surface buoys are equipped with four 140 W rated solar photovoltaic panels and two 350 W rated wind turbines, along with a rechargeable battery system inside the surface buoy. However, several factors impede the power output of these energy generation systems during extended deployment at sea. The solar panels experience reduced power output under periods of cloud cover or residual salt spray, while the wind turbines may suffer significant wear or damage due to various factors. As a result, the existing energy generation systems meet the full required power demand roughly 70% of the time. During periods of low energy supply, lower priority tasks are disabled to maintain overall system operation, limiting the full functionality of the observatory. This limitation motivates the need for additional power supply via a wave energy generation system.

An initial concept design report for such a device estimated that additional power of 10-20 W is sufficient to address this shortfall [4]. To this end, a number of bolt-on, small-scale power take-off (PTO) devices have been proposed that aim to not adversely affect the deployment process and data collection of the buoy. Specifically, the theory, analysis and experimental validation of an angular resonator was explored [5, 6]. The work herein builds upon this prior study to investigate a similar concept of an inverted pendulum resonator system and examine the degree to which nonlinearities affect device performance in various conditions. Equations of motion are derived and validated through the same bench-test platform, with modifications to accommodate the inverted pendulum configuration.

2 Inverted Pendulum: Concept and Model

2.1 Previous Designs

To understand the foundation of this work, it is important to define angular resonator wave energy converters (WECs). Angular resonator devices are categorized as floating pitching devices, in which energy is converted based on the relative rotation (mainly pitch) between two bodies [7]. These devices consist of three main parts: (i) a buoy that oscillates with waves, (ii) a rotating internal mass enclosed in the buoy, and (iii) a power take-off system that converts the relative motion between the buoy and the inertial mass into electrical energy [8, 9, 10]. By sealing the internal mass inside the main structure and reducing exposure to the ocean wave environment, the device's reliability may be improved. Devices in which the inner oscillating mass rotates about an axis inside the other body are known as pendulum devices, due to the fact that the device behaves mechanically equivalent to a pendulum [11].

Extensive research has been conducted on pendulum-based WECs. SEAREV (Système Électrique Autonome de Récupération d'Énergie des Vagues) is a proposed floating device with an enclosed hull that contains an oscillating pendulum to generate electricity [12]. The system allows for continuous rotations without endstops, improving the overall system's reliability [13]. PeWEC (passive inertial Pendulum Wave Energy Converter) follows a similar concept to extract power from damping the motion of a swinging pendulum in its enclosed hull [14, 15, 16]. WITT (Whatever Input Torque Transfer) uses a mechanical pendulum in a spherical hull to harvest energy in two perpendicular degrees of freedom [17]. These devices constitute a normal pendulum configuration, where the center of gravity is below the center of rotation.

Inverted pendulum systems, on the other hand, are devices with the center of mass above the center of rotation. This configuration has been shown through preliminary analysis to potentially better match the buoy's impedance, which would lead to more efficient energy transfer and therefore higher power performance. Given this strong advantage, the research herein investigates a numerical model for the inverted pendulum configuration to aid in characterizing its dynamics and thus power performance. The form of the model can be generalized to other angular resonator WECs. The following sections discuss the derivation of governing equations of motion of the system and experimental validation with data from a bench-test prototype.

2.2 Governing Equations of Motion for a Nonlinear Model

The full-scale system of the buoy with an inverted pendulum wave energy converter is shown in Figure 2a, and can be simplified into a double pendulum model as depicted in Figure 2b. The yellow body serves as a one degree-of-freedom swing to represent the buoy's pitching motion while the inverted pendulum rotates freely around a pin joint at a fixed location on the swing. Viscous friction at the swing and pendulum joints are modeled with linear damping elements, while Coulomb friction is represented as a constant, velocity-dependent opposing torque. The pendulum joint also contains a magnetic spring with a belt-drive transmission that provides a restoring torque, represented as a spring element in parallel with the damper. With this, the governing equations of motion for this configuration can be expressed as the following generic formulation:

$$\mathbf{M}\ddot{\mathbf{x}} + \mathbf{B}\dot{\mathbf{x}} + \mathbf{K}\mathbf{x} = \mathbf{T} \tag{1}$$

where $\mathbf{M} \in \mathbb{R}^{2\times2}$ represents the matrix of masses and moments of inertia for the system, $\mathbf{B} \in \mathbb{R}^{2\times2}$ is the viscous damping matrix, and $\mathbf{K} \in \mathbb{R}^{2\times2}$ is the restoring stiffness matrix. The state vector can be described as $\mathbf{x} = [\theta_1\ \theta_2]^T$ for the two degree of freedom system, where θ_1 and θ_2 denote the global angular position of the swing and pendulum respectively. $\mathbf{T} \in \mathbb{R}^{2\times1}$ denote the external torques experienced by the system.
The definitions of the matrices are given in the following:

$$\mathbf{M} = \begin{bmatrix} m_{11} & m_{12} \\ m_{21} & m_{22} \end{bmatrix}$$

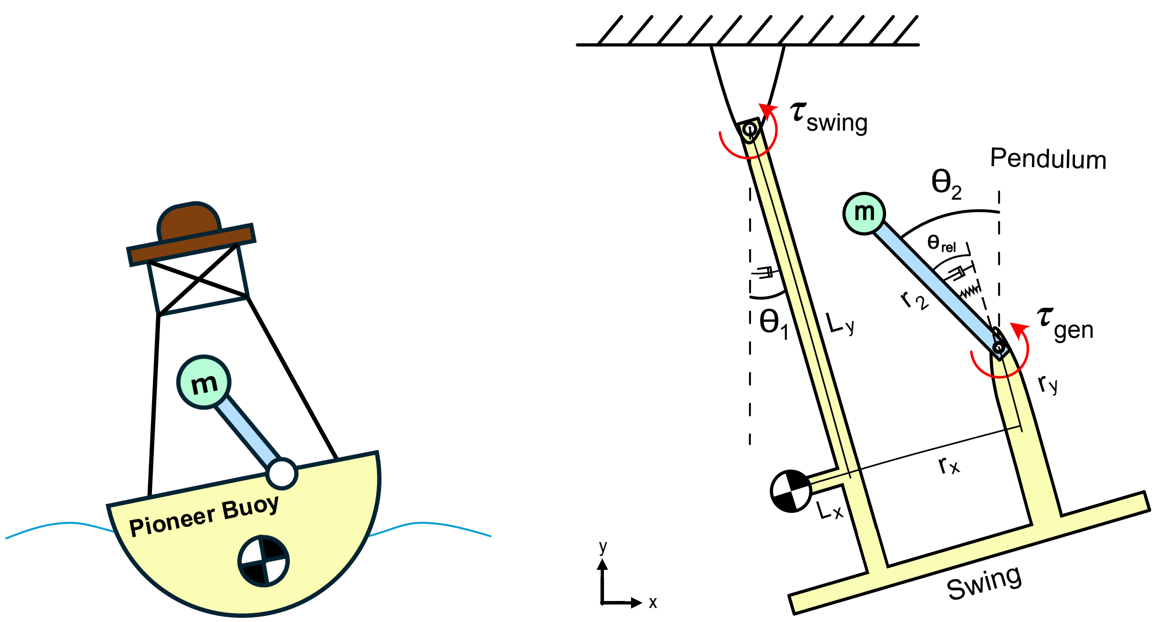

(a) Depiction of the inverted pendulum wave energy converter on the full-scale buoy.

(b) Simplified schematic of the inverted pendulum system in which governing equations of motion are derived.

Figure 2: Schematics of the inverted pendulum configuration.

where the mass and inertia coefficents are:

$$
\begin{aligned}
m_{11} &= J_1 + m_2 L_y^2 + m_2 r_x^2 + m_2 r_y^2 - 2 m_2 L_y r_y \\
m_{12} = m_{21} &= -m_2 L_y r_2 \cos(\theta_2 - \theta_1) \\
&\quad + m_2 r_y r_2 \cos(\theta_2 - \theta_1) - m_2 r_x r_2 \sin(\theta_2 - \theta_1) \\
m_{22} &= J_2
\end{aligned}
$$

$$
\mathbf{B} = \begin{bmatrix} b_{11} & b_{12} \\ b_{21} & b_{22} \end{bmatrix}
$$

where the damping coefficients are:

$$
\begin{aligned}
b_{11} &= b_1 + b_{rel} \\
b_{12} &= -b_{rel} + \dot{\theta}_2 (m_2 L_y r_2 \sin(\theta_2 - \theta_1) \\
&\quad - m_2 r_x r_2 \cos(\theta_2 - \theta_1) - m_2 r_y r_2 \sin(\theta_2 - \theta_1)) \\
b_{21} &= -b_{rel} + \dot{\theta}_1 (-m_2 L_y r_2 \sin(\theta_2 - \theta_1) \\
&\quad + m_2 r_x r_2 \cos(\theta_2 - \theta_1) + m_2 r_y r_2 \sin(\theta_2 - \theta_1)) \\
b_{22} &= b_{rel}
\end{aligned}
$$

$$
\mathbf{K} = \begin{bmatrix} N_2^2 k_{eq} & -N_2^2 k_{eq} \\ -N_2^2 k_{eq} & N_2^2 k_{eq} \end{bmatrix}
$$

where the stiffness coefficients are:

$$
{k_{eq}}^{-1} = {k_{backlash}}^{-1} + (k_{rel}(\theta_{mag}))^{-1}
$$

In the above equation, $k_{rel}(\theta_{mag})$ represents the relative spring stiffness as a function of magnetic spring angle displacement θ_{mag} as shown in Figure 4, where θ_{mag} is defined as following:

$$\theta_{mag} = N_2\theta_{pend} - \theta_s \tag{2}$$

The spring stiffness changes as a result of corresponding magnetic spring angle displacement θ_{mag}, which accounting for transmission, is equivalent to $N_2\theta_{pend}$. θ_s is incorporated to account for a difference in neutral angles between the magnetic spring and the pendulum, which arises due to the mass of the pendulum causing a drift from its natural vertical position. $k_{backlash}$ represents a stiffness that models the backlash and compliance of the belt-drive transmission. Together, these terms are treated as springs in series, hence the formulation of k_{eq}.

$$\mathbf{T} = \begin{bmatrix} t_1 \\ t_2 \end{bmatrix}$$

where the external torques are:

$$\begin{aligned} t_1 &= \tau_{swing} - N_1\tau_{gen} - m_1 g L_y \sin(\theta_1) + m_1 g L_x \cos(\theta_1) \\ &\quad - m_2 g L_y \sin(\theta_1) - m_2 g r_x \cos(\theta_1) + m_2 g r_y \sin(\theta_1) \\ &\quad - \tau_{col_1} + \tau_{col_2} \\ t_2 &= N_1\tau_{gen} + m_2 g r_2 \sin(\theta_2) - \tau_{col_2} \end{aligned}$$

τ_{col} denotes the Coulomb frictional torques and are calculated according to the equation listed below:

$$\tau_{col_i} = -\text{sign}(\dot{\theta}_i) * \mu_i \tag{3}$$

where μ_1 and μ_2 represents the Coulomb friction coefficient for the swing and pendulum respectively.

In the matrices above, J_1 and m_1, and J_2 and m_2, represent the lumped moments of inertia and masses of the swing and pendulum, respectively; b_1 and b_{rel} denote the lumped damping coefficients of the swing and pendulum acting proportional to relative velocity, respectively; k_{rel} represents the stiffness of the resonator spring.

In terms of positional coordinates, L_x and L_y represent the distance from the center of rotation to the swing's center of mass (COM) in the x and y direction respectively. Similarly, r_2 denotes the distance from the pendulum's center of rotation (pin joint) to its COM. r_x and r_y represent the distance from the swing's center of rotation to the pendulum's pin joint in the x and y direction respectively.

A transmission system was incorporated to optimize system performance. N_1 is the transmission ratio between the pendulum shaft and the generator shaft, while N_2 is the transmission ratio between the magnetic spring and the pendulum shaft. Both N_1 and N_2 will amplify the linear damping b_{rel} associated with the generator and spring, respectively, but since this term is treated as the overall lumped damping coefficient, the value will not be scaled by the transmissions. Since relative motion of a rotational joint in a physical system is more easily measured than the global motion, the experimental data will use output from the encoders to measure the relative angle θ_{rel} to inform the numerical model. This relative angle is defined as:

$$\theta_{rel} = \theta_2 - \theta_1 \tag{4}$$

2.3 Governing Equations of Motion for a Linear Model

The above nonlinear model was simplified into a linear model using small angle approximations and neglecting nonlinear terms, i.e. setting Coulomb friction to 0. The angles in the nonlinear model were simplified by the following equations:

$$\sin(\theta) \approx \theta \tag{5}$$

$$\cos(\theta) \approx 1 \tag{6}$$

Thus, the linear model was obtained and is presented in the following. The generic formulation remains the same, with the exception of matrix definitions.

$$\mathbf{M}_{linear} = \begin{bmatrix} m_{11} & m_{12} \\ m_{21} & m_{22} \end{bmatrix}$$

where the mass and inertia coefficents are:

$$\begin{aligned} m_{11} &= J_1 + m_2 L_y^2 + m_2 r_x^2 + m_2 r_y^2 - 2 m_2 L_y r_y \\ m_{12} = m_{21} &= -m_2 L_y r_2 + m_2 r_y r_2 \\ &\quad - m_2 r_x r_2 (\theta_2 - \theta_1) \\ m_{22} &= J_2 \end{aligned}$$

$$\mathbf{B}_{linear} = \begin{bmatrix} b_{11} & b_{12} \\ b_{21} & b_{22} \end{bmatrix}$$

where the damping coefficients are:

$$\begin{aligned} b_{11} &= b_1 + b_{rel} \\ b_{12} &= -b_{rel} + \dot{\theta}_2 (m_2 L_y r_2 (\theta_2 - \theta_1) - m_2 r_x r_2 \\ &\quad - m_2 r_y r_2 (\theta_2 - \theta_1)) \\ b_{21} &= -b_{rel} + \dot{\theta}_1 (-m_2 L_y r_2 (\theta_2 - \theta_1) + m_2 r_x r_2 \\ &\quad + m_2 r_y r_2 (\theta_2 - \theta_1)) \\ b_{22} &= b_{rel} \end{aligned}$$

$$\mathbf{K}_{linear} = \begin{bmatrix} N_2^2 k_{eq} & -N_2^2 k_{eq} \\ -N_2^2 k_{eq} & N_2^2 k_{eq} \end{bmatrix}$$

where the stiffness coefficients are:

$$k_{eq}{}^{-1} = k_{backlash}{}^{-1} + k_{avg}{}^{-1}$$

k_{avg} represents the average spring stiffness over the 0°- 45° range. It is calculated by fitting a linear slope to the spring torque graph across this range, and was found to be 50 Nm/rad.

$$\mathbf{T}_{linear} = \begin{bmatrix} t_1 \\ t_2 \end{bmatrix}$$

where the external torques are:

$$\begin{aligned} t_1 &= \tau_{swing} - N_1 \tau_{gen} - m_1 g L_y(\theta_1) + m_1 g L_x \\ &\quad - m_2 g L_y(\theta_1) - m_2 g r_x + m_2 g r_y(\theta_1) \\ t_2 &= N_1 \tau_{gen} + m_2 g r_2(\theta_2) \end{aligned}$$

3 Bench Test System

The numerical model was validated through a simple bench-top test system consisting of a small-scale version of the inverted pendulum with a one degree of freedom swing set to emulate pitching motion of the buoy, highlighted in Figure 3.

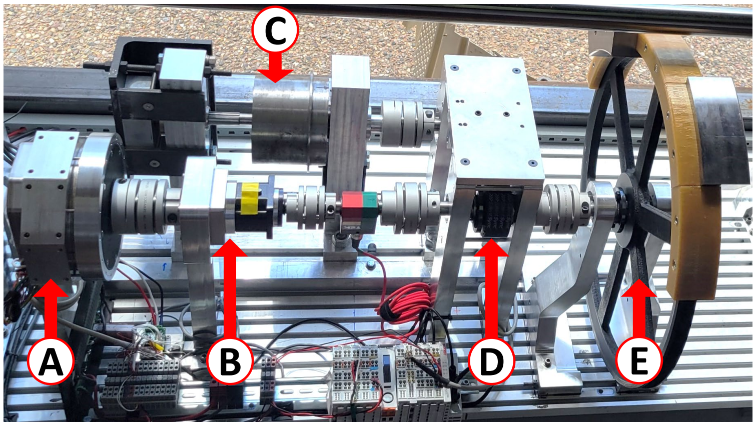

Figure 3: Physical setup of the bench top system with the inverted pendulum. Labeled components are as follows, A: generator, B: generator gear box, C: magnetic spring, D: belt drive, and E: inverted pendulum.

The experimental setup described in this paper builds upon the bench-test from a previous study [5], but introduces modifications to accommodate the inverted pendulum. This current system matches the schematic (Figure 2b) and consists of five main components. Figure 3 illustrates the complete system, which includes a motor/generator that produces τ_{gen}, a gearbox with transmission ratio N_2, a magnetic spring with stiffness K_{rel}, a belt drive with transmission ratio N_1, and a pendulum with inertia J_2. The motor/generator (Allied Motion's MF0150025C) is housed in a custom-built casing and operated by an Elmo motor controller (ELMO G-SOLTWI6/100EE7H) supplied with 48VDC. The generator transmission is a 3:1 planetary gearbox from Harmonic Drive (HPN-14A-03).

The magnetic spring can produce a peak torque of approximately 37 Nm, and behaves as a quasi-linear stiffness within the 0° to 45° displacement range, then transitions to a weakening spring in the 45° to 90° displacement range [18]. Beyond 90°, it behaves as an unstable spring, pushing the system to a new stable equilibrium that is 180° off from its initial position (Figure 4). Similar to the SEAREV design [12], the magnetic spring was chosen for its continuous travel between stable equilibria without any hard-stops. This could potentially mitigate shock loading on the buoy, and improve the safety of the device during storm conditions. A belt drive with transmission ratio 28:40 was placed between the pendulum and the magnetic spring, acting as a torque reducer from the magnetic spring to the inverted pendulum. The inverted pendulum consisted of steel segments placed on a custom-built pendulum to elevate its center of mass, and has a rotational inertia of 0.429 kgm^2. The components were joined using flexible shaft couplers to facilitate ease of assembly and alignment (see "E" in Figure 3).

The output of the magnetic spring was fitted with an 18-bit magnetic encoder (RLS MRA029BC010DSE00) for measurements of the relative angle, calculated through accounting for belt-drive transmission. This encoder was read in with a Beckhoff EL5042 card, communicating over BiSS-C. The output of the generator was read through a 19-bit encoder (RLS MRA039BC020DSE00). The generator encoder directly interfaced with the motor drive, which reported current, position, and velocity data. A ±50 Nm torque transducer (Futek FSH01989) was placed at the gearbox output and was read in by a 24-bit Beckhoff EL3356-0010.

The 1DOF swing set was controlled by an Allied Motion motor (Allied Motion MF0310100-C0X) in a custom housing. This motor was driven by a motor driver (Advanced Motion Controls DPEANIU-C100A400), and a 25 bit per revolution encoder (Heidenhain ENC425) provided position and velocity measurements. The motor drive communicated the motor's position, velocity, and current data. Additionally, a ±200 Nm torque transducer (Futek FSH01991) was installed between the swing drive motor and the swing set, read by another 24-bit Beckhoff EL3356-0010. A secondary 18-bit encoder (RLS MRA029BC010DSE00) was mounted on the back of the swing set to verify the swing angle and reduce measurement errors from shaft and/or coupling compliance. This encoder was also read using a Beckhoff EL5042 card that transmitted data over BiSS-C. Note that all sensors and drives communicated over EtherCAT, with a baseline real-time target machine running control in Simulink Real-Time[2]. All data from the system was

[2] https://www.mathworks.com/products/simulink-real-time.html

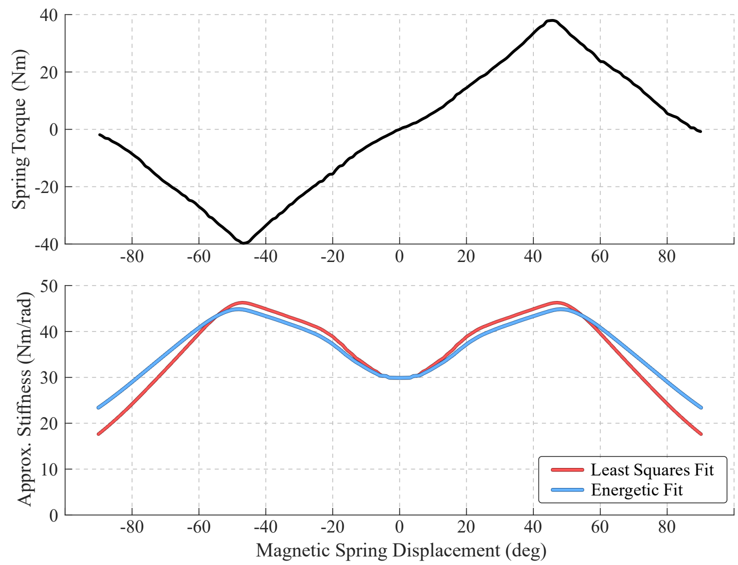

Figure 4: Plot of empirically measured magnetic spring torque and the corresponding spring stiffness approximations for displacement over ±90° range [5].

recorded at 1 kHz.

Estimates of the physical system parameters from the CAD model are shown in Table A.1 in Appendix A. Note that the reported inertias are the effective inertias of the whole system in the θ_{rel} coordinate frame. The reported spring stiffness is reflective of its stiffness over the entire ±45° range, but as seen in Figure 4, the spring stiffness varies for different oscillation ranges and cannot effectively represent the stiffness for the overall system. Additionally, the reported moments of inertia and masses are expected to be underestimated since the CAD models do not include components such as wires and the Beckhoff card stack.

4 Model Validation Methodology

System identification (SID) was performed using experimental data to estimate parameters in the nonlinear models. To obtain an initial estimate of the linear damping on each joint, single degree of freedom motion was applied on the swing set with the pendulum locked; and subsequently on the pendulum with the swing set locked. This approach prevented the dynamics of one degree of freedom from influencing the other, enabling a more accurate assessment of friction at the joint of interest. Thus, a 1DOF Swing nonlinear model, where the pendulum is locked on the swing, was used to assess friction at the swing joint. Using data from three multisine experiments, the swing parameters for the numerical model were estimated and then validated using a fourth, independent multisine trial. Similarly, a 1DOF Pendulum nonlinear model, where the swing is locked and the pendulum is free to rotate, was used to assess parameters at the pendulum joint. The pendulum parameters were estimated with three filtered white noise experiments and validated using a fourth trial. The results from the SID of 1DOF models then informed the 2DOF System nonlinear model which incorporated both degrees of freedom unlocked (see Figure 5 for an illustration of the workflow). Similar to the 1DOF cases, three multisine experiments with a fourth validation experiment were used to estimate parameters in the 2DOF model.

For SID of the 1DOF Swing nonlinear model, the system was excited with input of multisine current/torque commands at only the swing (τ_{exc}), while the 2DOF System nonlinear models were excited at both the swing (τ_{exc}) and generator motor (τ_{gen}). The variables in the state vector $\mathbf{x}$ and derivative $\dot{\mathbf{x}}$ (θ_1, θ_2, $\dot{\theta}_1$, $\dot{\theta}_2$) are measured in the experimental setup by the encoders on the swing and pendulum and used to compare against the numerical model.

The swing set is estimated to have a natural frequency of around 0.77 Hz, while the resonator has a natural frequency

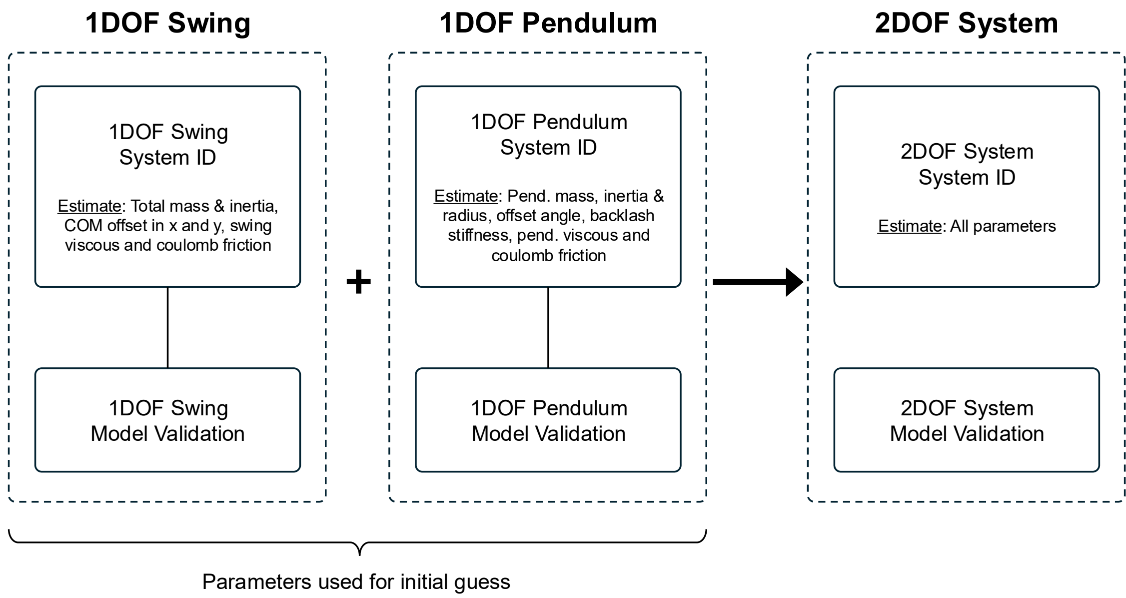

Figure 5: Diagram of the research workflow process. Each section denotes a separate numerical model, with the parameters estimated for the 1DOF Swing and 1DOF Pendulum models to inform the system identification of the overall 2DOF system model.

of around 0.3 Hz [5]. Based on these frequency values, the multisines were designed with frequency spectral content to broadly encapsulate both resonances and excite the system appropriately.

Two pink multisine signals, where amplitude components are inversely proportional to their frequencies, were generated that spanned a frequency range from 0.05 Hz to 2.5 Hz. To ensure independence of all inputs, these signals were created using pseudo-randomized phases. Additionally, to enhance signal-to-noise ratio, each input trial contained two and a half full periods of the multisine signals, with each period repeating every 300 s. The first pink multisine was amplified at a ratio of 5:4 relative to its original to generate a third signal, while the second pink multisine was amplified at a ratio of 3:4 relative to its original to generate a fourth signal. Due to the nonlinearity of the system, varying the gain of the multisine excitation signals still result in distinct and independent system responses across the experimental trials. Of these, three multisine signals were used as inputs to the nonlinear system identification, while the fourth signal was used as validation for the model.

For the 1DOF Pendulum model, narrow-banded, filtered white noise signals were also generated pseudo-randomly over a sample of 10 minutes for additional fidelity. A Butterworth bandpass filter was constructed that allowed frequencies between 0.1 -1.5 Hz to pass with minimal ripple of 1 dB, while attenuating frequencies below 0.1 Hz by 60 dB and frequencies above 2 Hz by 80 dB. This filter was then applied onto the white noise signal to obtain the desired frequency spectra. Similar to above, three white filtered noise signals were used as inputs for system identification, while the fourth served for the validation trial. For the generator, the torque gains were scaled to an average of 0 Nm across all four experiments, to keep the magnetic spring in the quasi-linear range of ±45° for the duration of the trial.

For these trials, the empirical data from torque transducers at the swing motor and gearbox were used as model inputs for SID, while the encoders at the back of the swing set and generator were used as model outputs. The Nonlinear Grey-Box Model software under the System Identification Toolbox[3] was used to perform the SID. The nonlinear grey-box model fits nonlinear differential equations with experimental data to estimate parameters in the equations using least-squares optimization algorithms.

[3] `https://www.mathworks.com/products/sysid.html`

5 Results

The results of the SID parameter estimations for the numerical models are shown in Table A.1. For each model, the table highlights the initial guesses of the parameter to use in the estimation, minimum and maximum bound restrictions, and the subsequent estimated value with percent error deviation from the initial guess. The rightmost column also contains notes that explain how the initial guesses were obtained. The percent error deviation was calculated via the below equation:

$$Error_{\%} = \frac{Estimated - Initial}{Initial} * 100 \tag{7}$$

such that a positive error indicates overestimation based on the initial guess, and a negative error indicates underestimation.

The fit percent of the nonlinear and linear model with tuned parameters compared against the experimental data are also highlighted in Table A.2. This fit percent depicts how well the numerical model approximates the experimental data, expressed as a percentage. The equation below calculates the fit percentage:

$$Fit_{\%} = 100 * \left(1 - \frac{||y_{exp} - y_{sim}||}{||y_{exp} - \text{mean}(y_{exp})||}\right) \tag{8}$$

where y_{exp} is the experimental data output, and y_{sim} is the simulation output. Note that a negative fit percent indicates that the model predictions are worse than using the mean of the experimental data for predictions.

The root mean square error (RMSE) values are depicted in Table A.3, showing average deviation of the numerical model from experimental results of the angles and velocities measured in deg or deg/sec.

For each model, sample time trajectories are presented to illustrate model predictions with the empirical data, as shown in Figure 6, Figure 9, and Figure 12. These plots compare the numerical model estimates against four experimental trials, with the tuned numerical model predictions of angles and velocities (shown in dashed red) and experimental data (shown in blue).

To quantify how well the linear model approximates the nonlinear model, single frequency sine signals of varying amplitudes and frequencies were input into the models to compute RMSE between the outputs (Figure 7 and Figure 10). The RMSE was taken after long intervals to ensure steady state conditions. For the 1DOF Swing model, Figure 7 shows that the model prediction errors are most pronounced in single sine simulations of high amplitude and ranges around the swing's natural frequency of 0.77 Hz. Similarly, the 1DOF Pend model shows higher error in the pendulum's resonant frequency, around 0.33 Hz (Figure 10). This may be due to the highly sensitive nature of the system at its resonant frequency, where any minor fluctuation will excite the system and amplify its output, leading to potentially high errors and poor predictions.

Additionally, the same signals were input into the model to measure the output's total harmonic distortion (THD), which illustrates the degree of harmonic distortion in a signal due to nonlinearities such as Coulomb friction (Figure 8 and Figure 11). At small amplitudes and frequencies, the system has near zero velocity, so nonlinearities such as Coulomb friction have a significantly larger effect on swing angle and velocity outputs. This is apparent in the data, as THD values are the highest for low amplitudes and frequencies.

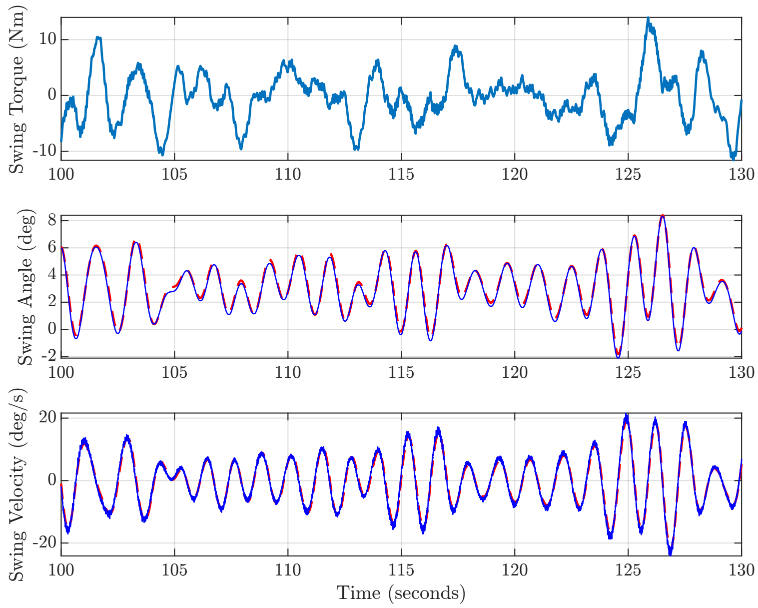

Figure 6: Sample time trajectories of the 1DOF Swing model for the validation trial over arbitrary time instants between 100 and 130 seconds. The above figures show the input swing torque, and an overlayed comparison of the model output for swing angle and swing velocity respectively (denoted with the red dashed line), against the corresponding experimental data (denoted with the solid blue line).

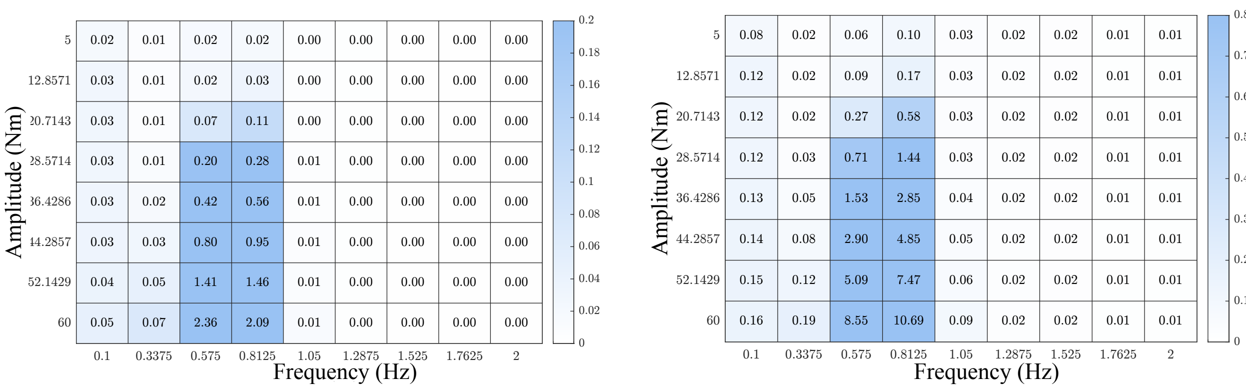

Figure 7: RMSE comparison of the nonlinear and linear models for the 1DOF Swing system undergoing single frequency sinusoidal torque inputs for (a) swing angle [deg] and (b) swing velocity [deg/s].

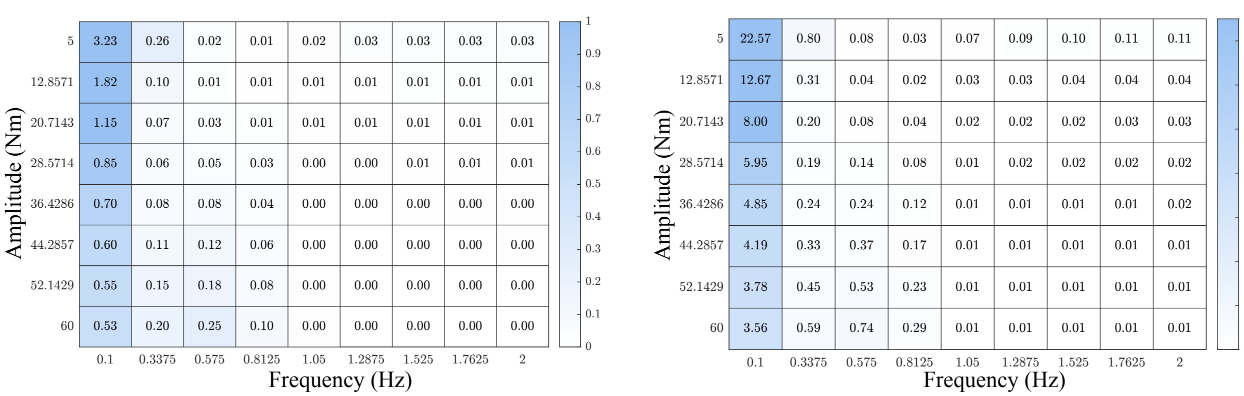

Figure 8: Total harmonic distortion of the nonlinear 1DOF Swing model for (a) swing angle [%] and (b) swing velocity [%].

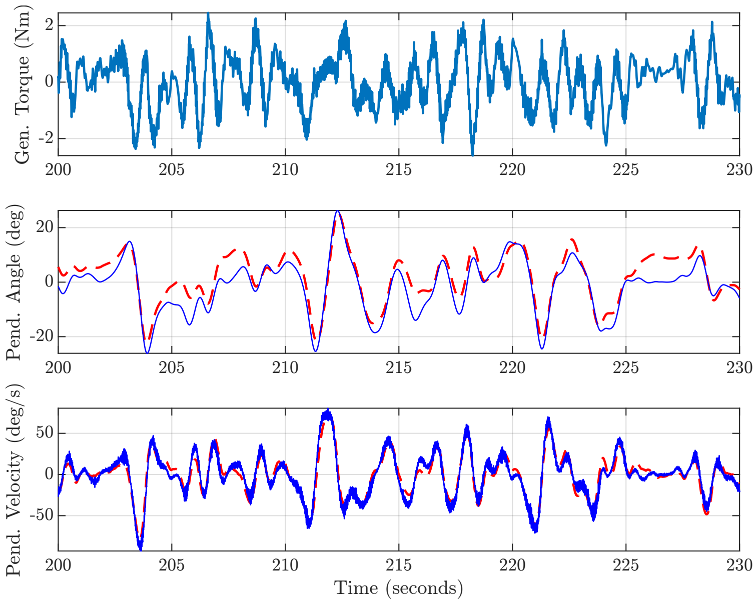

Figure 9: Sample time trajectories of the 1DOF Pend model for the validation trial over arbitrary time instants between 200 and 230 seconds. The above figures show the input generator torque, and an overlayed comparison of the model output for pendulum angle and velocity respectively (denoted with the red dashed line), against the corresponding experimental data (denoted with the solid blue line).

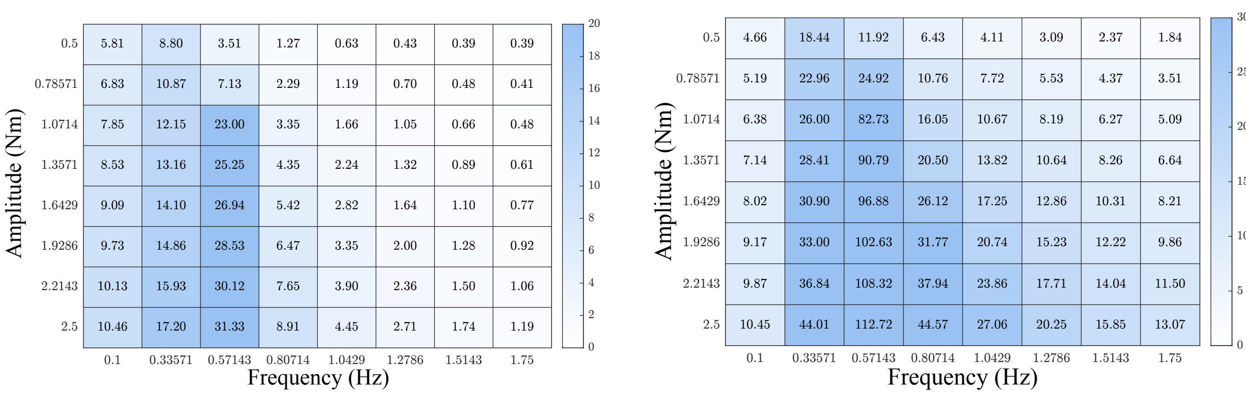

Figure 10: RMSE comparison of the nonlinear and linear models for the 1DOF Pend system undergoing single frequency sinusoidal torque inputs for (a) pendulum angle [deg] and (b) pendulum velocity [deg/s].

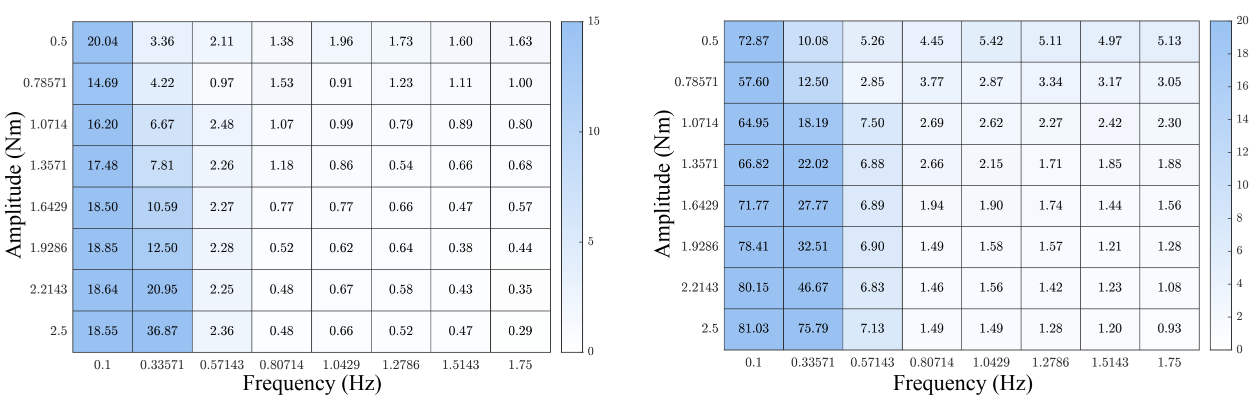

Figure 11: Total harmonic distortion of the nonlinear 1DOF Pendulum model for (a) pendulum angle [%] and (b) pendulum velocity [%].

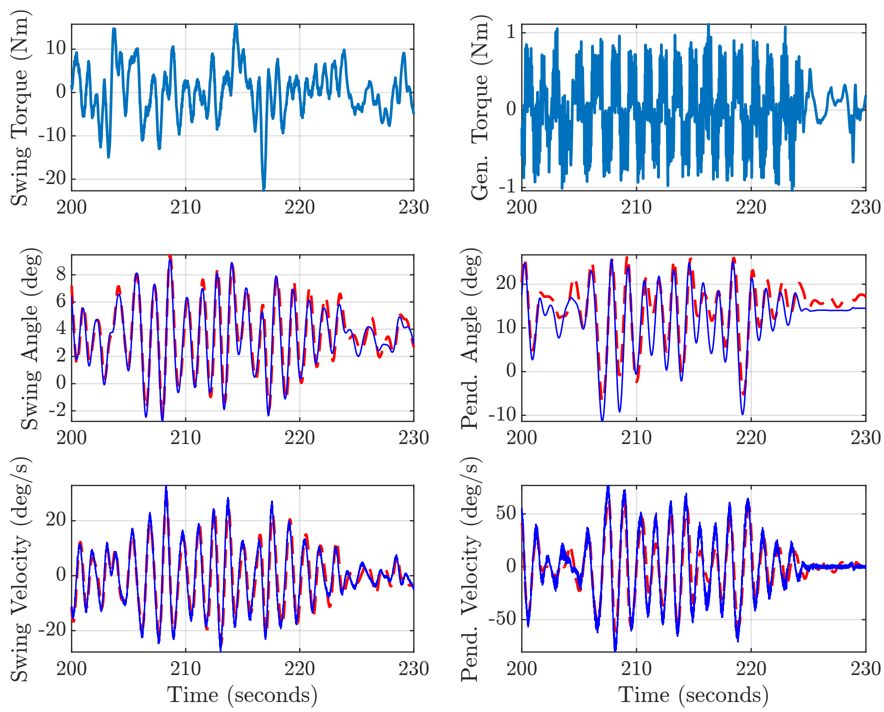

Figure 12: Sample time trajectories of the 2DOF System model for the validation trial over arbitrary time instants between 200 and 230 seconds. From left to right, and top to bottom, the figures highlight input swing and generator torques, with an overlayed comparison of the angles and velocities of the simulated model (denoted with the red dashed line) and the corresponding experimental data (denoted with the solid blue line).

6 Discussion

For the 1DOF Swing model, a nonlinear and a simplified linear model was generated for comparison. The nonlinear model yielded accuracies of 92.18% and 90.04% for swing angle and velocity, respectively, which shows strong performance and predictive capabilities. The linear model yielded an average of 45.74% and 44.76% for swing angle and velocity, respectively. As previously mentioned, the linear model assumes small-angle approximations and neglects nonlinearities such as Coulomb friction. Because of this, it is expected that the linear model will deviate significantly from the nonlinear model when the swing experienced large amplitudes of motion, or low frequencies in which system exhibits near-zero velocities and Coulomb friction dominates. The linear model will also fail to predict behavior at very low amplitudes which are insufficient to break Coulomb friction, since the linear model is unable to capture such nonlinearities. As apparent in the data, the RMSE increases with higher amplitude torque inputs and closer to the resonant frequency of around 0.77 Hz (Figure 7). At resonance, the projected swing angle often exceeded amplitudes of 15°, which would exceed the range where the small-angle assumptions hold. The RMSE at resonance peaks at 2.09 deg and 10.69 deg/s for the swing angle and velocity respectively, whereas non-resonant frequencies have RMSE of less than 0.05 deg and 0.19 deg/s for swing angle and velocity.

The 1DOF Pendulum models obtained less accurate results than the 1DOF Swing models (Table A.2). This lowered degree of accuracy could be due to the nonlinearity of the spring, or compliance and backlash from the belt-drive being not accurately captured by the model. Similar to the 1DOF Swing model, the 1DOF Pendulum model shows poor agreement for RMSE between the nonlinear and linear model in regions around the resonant frequency, and high amplitudes (Figure 10). The THD is also more apparent when Coulomb friction dominates, at low frequencies and low amplitudes (Figure 11). This suggests that the linear 1DOF Pendulum model approximates the system better in non-resonant frequencies and amplitudes that avoid the Coulomb friction regime. Additional improvements to the model involve better characterizing the spring stiffness for backlash and compliance via conducting characterization tests on stiffness measures for a more precise estimate.

The 2DOF System model obtained average results of 76.7% for the swing angle, 77.2% for the swing velocity, 58.5% for the pendulum angle, and 61.76% for the pendulum velocity. The nonlinear models approximate the system adequately, but the linear model only approximates the swing angle and velocities to accuracies of 30%, and significantly deteriorates for the pendulum outputs. The linear model tends to yield a high degree of error at the resonant frequency, in which it over-predicts the dynamics and fails to approximate the system accurately beyond the resonant point. Thus, similar to before, the 2DOF models approximate the system well for low amplitudes and for non-resonant frequencies. It is of note that the above nonlinear models approximate friction as the sum of linear (viscous) and Coulomb (constant) friction, whereas in reality, some amount of friction will have a quadratic relationship with velocity that is not incorporated in the models. Thus, to improve upon the models, a more accurate characterization of friction can be considered for higher confidence estimates.

7 Conclusion

This paper explores an inverted pendulum concept for a wave energy converter to power oceanographic buoys in the Coastal Pioneer Array. Nonlinear numerical models of the system are defined through deriving governing equations of motions. A simplified linear model can also be obtained using small angle approximations and neglecting Coulomb friction of the nonlinear model, which can save computation time and enable a broader range of analysis techniques while approximating the nonlinear model with a high degree of accuracy. The above models were then validated against experimental data obtained from a prototype bench-test replica. System identification was used to estimate the parameters in the models (i.e., the viscous damping coefficients and friction parameters etc) using repeating multisine and filtered, white noise input torques.

To compare the nonlinear and linear model, RMSE between the outputs was computed. THD was used to quantify the nonlinearities present in the nonlinear model. From these analyses, the linear model showed more disagreement with the nonlinear model for high amplitudes and frequencies near resonance. The nonlinear model also exhibited significant nonlinearities for lower frequencies and amplitudes, likely due to static and Coulomb friction that arises during initial movements. This indicates that friction plays a pronounced role in near-zero frequencies and amplitudes, and highlights the importance of capturing nonlinearities in these conditions. Thus, the linear model can be adequately applied for frequencies outside of the resonant frequency and amplitudes that allow for small angle approximation but avoid the regime where Coulomb friction dominates.

These numerical models provide a means to approximate the dynamics of the system for rapid design iteration and selection for the full-scale system. In quantifying the conditions where the linear model approximates the nonlinear model, the linear model can be appropriately applied to reduce computational complexity and improve efficiency in the design process. Future work will involve improving the 1DOF pendulum model and investigating additional nonlinearities that may arise when scaling up to the full-scale buoy.

Acknowledgments

The authors would like to acknowledge funding support from the US Department of Energy's Water Power Technologies Office. Sandia National Laboratories is a multi-mission laboratory managed and operated by National Technology and Engineering Solutions of Sandia, LLC., a wholly owned subsidiary of Honeywell International, Inc., for the U.S. Department of Energy's National Nuclear Security Administration under contract DE-NA0003525. This paper describes objective technical results and analysis. Any subjective views or opinions that might be expressed in the paper do not necessarily represent the views of the U.S. Department of Energy or the United States Government.

Appendix A. Comparison of Numerical Models

Table A.1: Physical system parameters estimated from system identification experiments.

		Initial Value	Min. Bound	Max. Bound	Estimated Value	Deviation (%)	
1DOF Swing Model	Total Swing and Pendulum Mass, m_{tot} [kg]	92.91	75	105	100.34	7.99	Estimates from CAD
	Total Moment of inertia, J_{tot} [kg m^2]	14.488	14	18	17.74	22.46	Estimates from CAD
	Swing Distance to COM y-direction, L_y [m]	0.333	0.32	0.36	0.359	7.82	Estimates from CAD
	Swing Distance to COM x-direction, L_x [m]	0.0178	0.01	0.1	0.0199	12.02	Estimates from CAD
	Swing Viscous Friction, B_1 [Nms/rad]	0.08	0.005	3	0.0885	10.61	Estimates from Decay Test SysID
	Swing Coulomb Friction, τ_{col_1} [Nm]	0.04	0.005	2	0.0402	0.45	Estimates from Decay Test SysID
1DOF Pendulum Model	Pend. Mass, m_2 [kg]	13.91	13	15	13.46	-3.22	Estimates from Physical Measurement
	Pend. Moment of inertia, J_2 [kg m^2]	0.437	0.4	0.65	0.494	12.98	Estimates from CAD
	Pend. radius, r_2 [m]	0.09	0.075	0.12	0.0878	-2.43	Estimates from Physical Measurement
	Pend. Viscous Friction, B_2 [Nms/rad]	0.2	0.001	3	0.207	3.76	Estimates from Decay Test SysID
	Pend. Coulomb Friction, τ_{col_2} [Nm]	0.1	0.001	3	0.149	49.01	Estimates from Decay Test SysID
	Stiffness from backlash, $k_{backlash}$ [Nm/rad]	2000	100	1e5	2256.3	12.82	Estimates from Decay Test SysID
	Offset angle from belt-drive, θ_s [deg]	0.1	-2	2	0.0407	-59.3	Estimates from Decay Test SysID
2DOF System Model	Swing Mass, m_1 [kg]	84.5	78.5	102.7	84.12	-0.45	Estimates from 1DOF Swing Model
	Swing Moment of inertia, J_1 [kg m^2]	16.2	13.6	17.5	16.25	0.30	Estimates from 1DOF Swing Model
	Swing Distance to COM y-direction, L_y [m]	0.382	0.362	0.47	0.384	0.58	Estimates from 1DOF Swing Model
	Swing Distance to COM x-direction, L_x [m]	0.0289	0.0	0.052	0.0290	0.18	Estimates from 1DOF Swing Model
	Distance to pin joint from swing rotation center y-direction, r_y [m]	0.102	0.1	0.133	0.103	1.33	Estimates from 1DOF Swing Model
	Distance to pin joint from swing rotation center x-direction, r_x [m]	0.045	0.03	0.059	0.040	-10.78	Estimates from 1DOF Swing Model
	Swing Viscous Friction, B_1 [Nms/rad]	0.1	0.01	1	0.087	-13.15	Estimates from Decay Test SysID
	Swing Coulomb Friction, τ_{col_1} [Nm]	0.09	0.001	1	0.087	-3.62	Estimates from Decay Test SysID
	Pend. Mass, m_2 [kg]	13.85	13.2	14.75	14.022	1.24	Estimates from Physical Measurement
	Pend. Moment of inertia, J_2 [kg m^2]	0.465	0.425	0.585	0.451	-2.98	Estimates from CAD
	Pend. radius, r_2 [m]	0.095	0.08	0.11	0.095	0	Estimates from 1DOF Pend Model
	Pend. Viscous Friction, B_2 [Nms/rad]	0.1	0.01	2	0.162	61.58	Estimates from Decay Test SysID
	Pend. Coulomb Friction, τ_{col_2} [Nm]	0.2	0.01	1	0.133	-33.4	Estimates from Decay Test SysID
	Stiffness from backlash, $k_{backlash}$ [Nm/rad]	8000	100	1e05	7591.8	-5.10	Estimates from Decay Test SysID
	Offset angle from belt-drive, θ_s [deg]	0.46	-1.5	1.5	0.44	-4.5	Estimates from Decay Test SysID

Table A.2: Summary of all nonlinear and linear model fit percents. The table highlights the model accuracy for angle and velocity across three experiments used to train the numerical model, along with the fourth validation experiment and the corresponding average across all experiments.

		Trained Experiments Average Fit Percent (%)	Validation Experiment Fit Percent (%)
1DOF Swing Model	Nonlinear Model Accuracy for Swing Angle	92.08	92.47
	Linear Model Accuracy for Swing Angle	40.81	60.54
	Nonlinear Model Accuracy for Swing Velocity	89.81	90.71
	Linear Model Accuracy for Swing Angle	39.66	60.06
1DOF Pend Model	Nonlinear Model Accuracy for Pend Angle	55.22	46.19
	Linear Model Accuracy for Pend Angle	7.63	6.38
	Nonlinear Model Accuracy for Pend Velocity	65.15	63.99
	Linear Model Accuracy for Pend Velocity	4.60	4.53
2DOF System Model	Nonlinear Model Accuracy for Swing Angle	74.52	78.6
	Linear Model Accuracy for Swing Angle	-10.53	-0.95
	Nonlinear Model Accuracy for Swing Velocity	77.09	78.17
	Linear Model Accuracy for Swing Velocity	-4.63	4.14
	Nonlinear Model Accuracy for Pend Angle	43.12	46.35
	Linear Model Accuracy for Pend Angle	-109.38	-132.99
	Nonlinear Model Accuracy for Pend Velocity	67.83	65.80
	Linear Model Accuracy for Pend Velocity	-58.82	-81.00

Table A.3: Summary of RMS Error in nonlinear and linear models for 1DOF Swing, 1DOF Pendulum, 2DOF System.

		Trained Experiments Average	Validation Experiment
1DOF Swing Model	Nonlinear Model RMS for Swing Angle [deg]	0.41	0.23
	Linear Model RMS for Swing Angle [deg]	3.13	1.18
	Nonlinear Model RMS for Swing Velocity [deg/s]	2.35	1.24
	Linear Model RMS for Swing Velocity [deg/s]	14.09	5.29
1DOF Pendulum Model	Nonlinear Model RMS for Pend. Angle [deg]	4.28	5.09
	Linear Model RMS for Pend. Angle [deg]	8.83	8.82
	Nonlinear Model RMS for Pend. Velocity [deg/s]	9.11	9.60
	Linear Model RMS for Pend. Velocity [deg/s]	24.99	24.97
2DOF System Model	Nonlinear Model RMS for Swing Angle [deg]	0.37	0.42
	Linear Model RMS for Swing Angle [deg]	1.76	1.96
	Nonlinear Model RMS for Swing Velocity [deg/s]	1.51	1.91
	Linear Model RMS for Swing Velocity [deg/s]	7.53	8.41
	Nonlinear Model RMS for Pend. Angle [deg]	3.39	3.06
	Linear Model RMS for Pend. Angle [deg]	12.89	13.30
	Nonlinear Model RMS for Pend. Velocity [deg/s]	7.05	7.48
	Linear Model RMS for Pend. Velocity [deg/s]	37.71	39.65

References

[1] Glen Gawarkiewicz and Albert J. Plueddemann. “Scientific rationale and conceptual design of a process-oriented shelfbreak observatory: the OOI Pioneer Array”. In: *Journal of Operational Oceanography* 13.1 (2020), pp. 19–36. DOI: `10.1080/1755876X.2019.1679609`. eprint: `https://doi.org/10.1080/1755876X.2019.1679609`. URL: `https://doi.org/10.1080/1755876X.2019.1679609`.

[2] Matthew Palanza, Stephanie Petillo, and Paul Matthias. “Ocean observatories initiative coastal surface mooring technology”. In: *OCEANS 2017 - Aberdeen*. 2017, pp. 1–4. DOI: `10.1109/OCEANSE.2017.8085008`.

[3] Donald B. Peters, John N. Kemp, and Albert J. Plueddemann. “Coastal surface mooring developments for the Ocean Observatories Initiative (OOI)”. In: *Marine Technology Society Journal* 56.6 (2022), pp. 70–74. DOI: `10.4031/MTSJ.56.6.2`.

[4] Ryan G. Coe et al. "Pioneer WEC concept design report". In: (Oct. 2023). DOI: 10.2172/2280833. URL: https://www.osti.gov/biblio/2280833.

[5] J. Lee, A. Keow, R.G. Coe, et al. "Theory, Analysis, and Testing of an Angular Resonator for Wave Energy Generation". In: *Journal of Ocean Engineering and Marine Energy* 11 (2025), pp. 97–107. DOI: 10.1007/s40722-024-00366-6. URL: https://doi.org/10.1007/s40722-024-00366-6.

[6] Ryan Coe et al. *Bench Testing Data and Report for an Early Prototype Pitch Resonator WEC*. Marine and Hydrokinetic Data Repository, Sandia National Laboratories, https://doi.org/10.15473/2475742. Accessed: 2025-06-04. 2024. DOI: 10.15473/2475742. URL: https://mhkdr.openei.org/submissions/558.

[7] Tunde Aderinto and Hua Li. "Ocean Wave Energy Converters: Status and Challenges". In: *Energies* 11.5 (2018). ISSN: 1996-1073. DOI: 10.3390/en11051250. URL: https://www.mdpi.com/1996-1073/11/5/1250.

[8] António F. de O. Falcão. "Wave energy utilization: A review of the technologies". In: *Renewable and Sustainable Energy Reviews* 14.3 (2010), pp. 899–918. ISSN: 1364-0321. DOI: https://doi.org/10.1016/j.rser.2009.11.003. URL: https://www.sciencedirect.com/science/article/pii/S1364032109002652.

[9] Jinming Wu. "On Power-Absorption Degrees of Freedom for Point Absorber Wave Energy Converters". In: *Journal of Marine Science and Engineering* 8.9 (2020). ISSN: 2077-1312. DOI: 10.3390/jmse8090711. URL: https://www.mdpi.com/2077-1312/8/9/711.

[10] Yong Ma et al. "Hydrodynamic Performance of a Pitching Float Wave Energy Converter". In: *Energies* 13.7 (2020). ISSN: 1996-1073. DOI: 10.3390/en13071801. URL: https://www.mdpi.com/1996-1073/13/7/1801.

[11] Xiaoqiang Jiang et al. "System analysis and experimental investigation of a pendulum-based wave energy converter". In: *Ocean Engineering* 277 (2023), p. 114300. ISSN: 0029-8018. DOI: 10.1016/j.oceaneng.2023.114300. URL: https://www.sciencedirect.com/science/article/pii/S0029801823006844.

[12] Alain Clément et al. "The SEAREV wave energy converter". In: *Proceedings of the 6th Wave and Tidal Energy Conference, Glasgow, UK* (Jan. 2005).

[13] J. Cordonnier et al. "SEAREV: Case study of the development of a wave energy converter". In: *Renewable Energy* 80 (2015), pp. 40–52. ISSN: 0960-1481. DOI: https://doi.org/10.1016/j.renene.2015.01.061. URL: https://www.sciencedirect.com/science/article/pii/S0960148115000798.

[14] G. Rinaldi et al. "Development of a simplified analytical model for a passive inertial system solicited by wave motion". In: *International Journal of Marine Energy* 13 (2016), pp. 45–61. ISSN: 2214-1669. DOI: https://doi.org/10.1016/j.ijome.2015.10.003. URL: https://www.sciencedirect.com/science/article/pii/S2214166915000375.

[15] Nicola Pozzi et al. "PeWEC: Experimental validation of wave to PTO numerical model". In: *Ocean Engineering* 167 (2018), pp. 114–129. ISSN: 0029-8018. DOI: https://doi.org/10.1016/j.oceaneng.2018.08.028. URL: https://www.sciencedirect.com/science/article/pii/S0029801818315233.

[16] Sergej Antonello Sirigu et al. "Techno-Economic Optimisation for a Wave Energy Converter via Genetic Algorithm". In: *Journal of Marine Science and Engineering* 8.7 (2020). ISSN: 2077-1312. DOI: 10.3390/jmse8070482. URL: https://www.mdpi.com/2077-1312/8/7/482.

[17] S. Crowley et al. "Modelling of the WITT wave energy converter". In: *Renewable Energy* 115 (2018), pp. 159–174. ISSN: 0960-1481. DOI: https://doi.org/10.1016/j.renene.2017.08.004. URL: https://www.sciencedirect.com/science/article/pii/S0960148117307565.

[18] Dawei Che et al. "A Multi-Stack Variable Stiffness Magnetic Torsion Spring for a Wave Energy Converter". In: *2022 IEEE Energy Conversion Congress and Exposition (ECCE)*. 2022, pp. 1–6. DOI: 10.1109/ECCE50734.2022.9947751.